

Accuracy Does Not Guarantee Human-Likeness in Monocular Depth Estimators

Yuki Kubota

Communication Science Laboratories, NTT, Inc.
3-1 Morinosato-Wakamiya, Atsugi-shi, Kanagawa, 243-0198
yuki.kubota95@gmail.com

Taiki Fukiage

Communication Science Laboratories, NTT, Inc.
3-1 Morinosato-Wakamiya, Atsugi-shi, Kanagawa, 243-0198
t.fukiage@gmail.com

Abstract

Monocular depth estimation is a fundamental capability for real-world applications such as autonomous driving and robotics. Although deep neural networks (DNNs) have achieved superhuman accuracy on physical-based benchmarks, a key challenge remains: aligning model representations with human perception, a promising strategy for enhancing model robustness and interpretability. Research in object recognition has revealed a complex trade-off between model accuracy and human-like behavior, raising a question whether a similar divergence exist in depth estimation, particularly for natural outdoor scenes where benchmarks rely on sensor-based ground truth rather than human perceptual estimates. In this study, we systematically investigated the relationship between model accuracy and human similarity across 69 monocular depth estimators using the KITTI dataset. To dissect the structure of error patterns on a factor-by-factor basis, we applied affine fitting to decompose prediction errors into interpretable components. Intriguingly, our results reveal while humans and DNNs share certain estimation biases (positive error correlations), we observed distinct trade-off relationships between model accuracy and human similarity. This finding indicates that improving accuracy does not necessarily lead to more human-like behavior, underscoring the necessity of developing multifaceted, human-centric evaluations beyond traditional accuracy.

1. Introduction

Monocular Depth Estimation (MDE) infers three-dimensional (3D) structure from a single RGB image and is a core computer vision problem with broad impact in applications such as autonomous driving and

robotics. MDE models have achieved remarkable progress, driven by advancements from convolution-based [11] to Transformer-based [35, 44, 67] and generative-based architectures [22, 31], alongside sophisticated generalization strategies like training on large, mixed datasets [7, 40] and self-supervised learning [49, 68]. Consequently, current deep neural networks (DNNs) have already surpassed human performance when evaluated on standard physically based benchmarks [27].

However, despite this measured superiority, ensuring the model’s robustness (particularly to out-of-distribution data) and interpretability remains a critical, open challenge. One promising approach to this challenge is aligning model representations with human visual perception, as human-like representations are often more resistant to distortions and adversarial perturbations [12, 15, 48, 56]. Such representational alignment would yield more adaptive and generalizable visual reasoning [18, 20, 39]. This pursuit of human-likeness naturally raises a fundamental question about its relationship with model accuracy. Early alignment studies in object recognition suggested a positive correlation [59], but later research revealed more nuanced pictures, including systematic divergences such as the shape-texture bias [14] and a potential trade-off between high accuracy and human-like behavior [9, 19, 29].

This alignment-focused research has recently expanded beyond object recognition to spatial and intermediate representations [1, 27, 37, 42, 62, 63]. In the context of depth estimation, however, progress has been constrained by the absence of datasets enabling direct comparison between human and DNN depth estimations grounded in physical measurements. Although some datasets incorporate human evaluations [8, 32], these datasets regard human data as pseudo-ground truth, collected to fill missing sensor measurements rather than to systematically investigate human

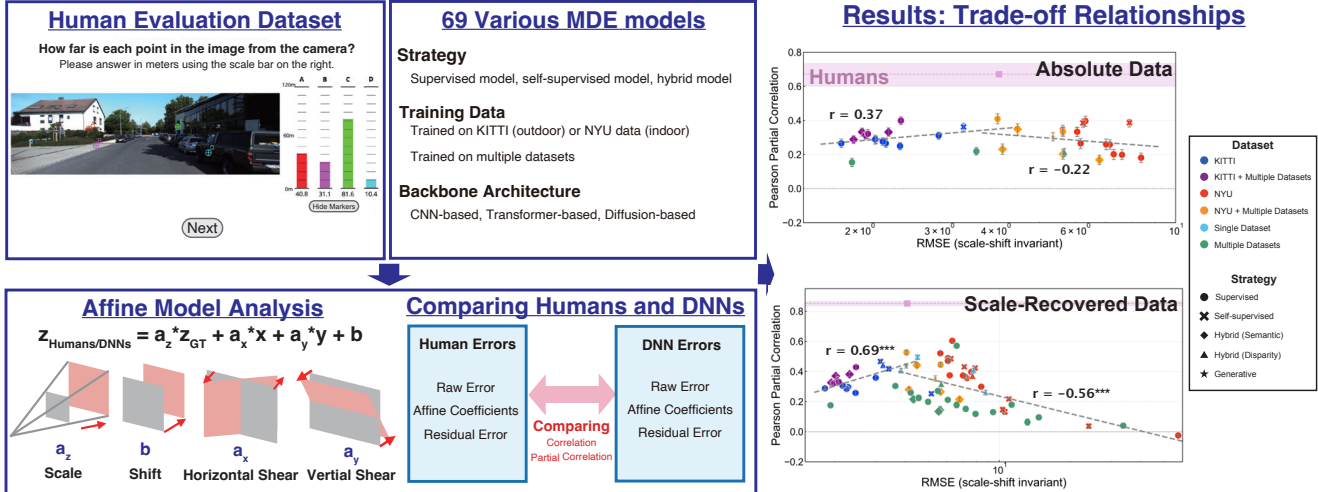


Figure 1. Overview of our research. We first constructed a human depth evaluation dataset based on an absolute depth estimation task. Next, we recruited 69 pre-trained deep neural networks (DNNs) for monocular depth estimation and compared their depth estimation errors with human evaluations using partial correlation analysis. We found trade-off relationships between model accuracy (horizontal axis) and human similarity of error patterns (vertical axis). To further disentangle the sources of these errors, we conducted an affine decomposition, evaluating systematic, per-image distortions of humans and DNNs (* : $p < 0.01$, ** : $p < 0.01$, and *** : $p < 0.001$).

perceptual biases or model alignment.

The recent emergence of datasets combining perceptual and physical depth information has begun to close this gap. A recent study constructed an indoor human depth evaluations using NYU Depth V2 [46]. They reported that higher-accuracy monocular depth estimators tend to exhibit certain human-like biases, such as depth compression and per-image affine distortions [27]. However, it remains unclear whether this tendency is domain-specific or reflects a more general characteristic of depth estimation models. More critically, in light of findings from object recognition, it remains an open question whether a trade-off relationship between accuracy and human-likeness emerges in depth estimation.

To address this gap, we investigate how model accuracy relates to human-likeness in outdoor depth estimation. We collected new human-annotated depth dataset for the widely used KITTI benchmark [50] and compared error structures across 69 MDE models. Extending the affine decomposition framework from prior work [27], we dissected human-DNN error relationships into interpretable components. Our findings reveal a consistent trade-off between metric depth estimation accuracy and similarity to human behavior, suggesting that highly accurate models may achieve their superior performance by employing strategies that are divergent from the human visual system. It demonstrates that the pursuit of metrically superior models alone is insufficient for creating models with human-like representations and estimation strategies. Human-centric evaluation constitutes a critical new avenue for assessing model validity underlying

estimation strategies, moving beyond traditional accuracy metrics to gauge perceptual alignment.

The collected dataset and analysis code will be released publicly alongside this paper to facilitate further research on human-AI alignment in depth estimation.

2. Related work

Evaluating monocular depth estimation models: Evaluation methodologies for MDE have evolved alongside the models themselves, primarily focusing on metric accuracy. Early supervised methods, trained on datasets like NYU Depth V2 [46] and KITTI [50], established a suite of standard error metrics such as AbsRel and RMSE to quantify per-pixel depth accuracy [11]. However, a key challenge is that monocular predictions are inherently scale-ambiguous. To address this, a common practice is to apply a per-image alignment—typically median scaling or least-squares fitting—before computing errors, ensuring a fair comparison even for models that do not output metric depth [11, 43]. More recently, zero-shot cross-dataset evaluation has become central for assessing out-of-distribution robustness, especially for large, mixed-data foundation models (e.g., [61]). While these metrics effectively quantify accuracy, an emerging perspective is to align models with human perception to enhance robustness. Supporting this view, a recent study by Bae et al. [1] reported a positive relationship between model robustness and the strength of shape-texture bias—a behavioral hallmark of human object recognition. However, model evaluation remains predominantly tied to physically measured ground

truth (e.g., LiDAR). In contrast, our work proposes a novel evaluation framework for the depth estimation task, benchmarked against human depth estimates, offering complementary insights into model behaviors beyond conventional accuracy metrics.

Human-annotated depth datasets: A key strategy for model alignment has been to leverage human judgments, especially ordinal comparisons that reflect how people naturally assess spatial relationships. This approach is motivated by the psychophysical finding that humans are often more reliable at making relative judgments (e.g., “which point is closer?”) than estimating absolute metric values. Pioneering work by Zoran et al. [70] established a framework to train models directly from such pairwise ordinal data. This line of inquiry was significantly advanced by the Depth in the Wild (DIW) dataset [8], which introduced the large-scale use of human judgments on relative ordinal depth to evaluate models on diverse in-the-wild images. Subsequent studies have leveraged similar human-annotated ordinal and occlusive cues to guide model training [32]. However, a crucial limitation of these datasets is the lack of coupled physical ground truth and human perceptual estimates for the same scenes. This absence of paired data, combined with their focus on ordinal tasks, prevented a direct quantitative comparison of metric error patterns between humans and DNNs. A recent study [27] began to close this gap. They developed a methodology for reliably collecting absolute depth judgments from human observers, creating the first dataset suitable for such a direct comparison. Using this, they analyzed estimation errors on an indoor dataset (NYU) and reported a positive correlation where higher-accuracy models exhibited more human-like biases. Our work extends this investigation to an outdoor domain (KITTI). By employing a detailed affine decomposition of error patterns, we uncover a distinct inverse-U relationship, suggesting that the pursuit of superhuman metric accuracy can force models to adopt strategies that diverge from those of the human visual system.

Human depth perception: Research on human depth perception has shifted from treating the visual system as a veridical estimator of physical depth [30] to emphasizing its systematic, context-dependent distortions from the physical depth structure [38, 55]. These biases are thought to arise because the visual system relies on learned statistical priors to resolve the ambiguity inherent in projecting the 3D world onto 2D retinal images [64]. An influential framework posits that perceived space does not follow a veridical metric but adheres to an affine geometry, which preserves local shape consistency while allowing for global distortions such as scaling and shearing [25, 51, 53]. This perspective reframes perceptual biases not as failures of the visual system, but as adaptive consequences of its processing strategies. The standard MDE evaluation protocol of

per-image scale and shift alignment can be seen as a simplified application of this principle, as it accounts for a subset of affine transformations. Building on this view, we adopt affine-based analysis to decompose and compare the error structures of human and DNN depth estimations.

3. Methods

3.1. Human depth evaluation for KITTI dataset

To directly compare depth estimation between humans and DNNs under identical conditions, we collected human depth evaluations through a psychophysical experiment. As stimulus images, we randomly selected 328 scenes from the KITTI dataset—the most widely used benchmark for outdoor depth estimation [50]. The KITTI dataset is an RGB-D dataset constructed from LiDAR measurements and synchronized on-vehicle cameras. Because all images were captured from a roof-mounted camera, both the intrinsic parameters and the relative camera pose within the vehicle coordinate system almost remained constant.

Previous studies have often relied on two-alternative forced-choice (2AFC) paradigms or relative depth ordering tasks [8, 32, 53], which are unsuitable for comparing error patterns against metric ground truth. Therefore, in our experiment, participants were asked to report the *absolute distance* (in meters) from the camera to specific evaluation points within each image (see “Human Evaluation Dataset” in Figure 1). To enhance the reliability of these absolute estimates, we designed the task such that participants estimated four points simultaneously within each image. Presenting multiple points together provided a relational context, stabilizing absolute depth estimates by allowing participants to compare and calibrate their estimates across points. This methodological choice is supported by prior findings showing that absolute depth estimates yield internally consistent correlations with both ordinal and relative depth judgments [27].

Unlike DNNs, which output dense depth maps, it is unrealistic to expect humans to provide pixel-wise estimates. To balance experimental feasibility with comparability to DNNs, we defined 16 evaluation points per image, randomly sampled under the constraint that candidate points and image edges (or segmentation boundaries) were separated by a certain minimum distance (see Appendix A.1). In practice, the 16 evaluation points were divided into four groups, and participants judged four points simultaneously within the same image.

Human depth evaluations were collected via a crowdsourcing platform from 890 participants in their 20s to 40s. Each experiment lasted approximately 20 minutes, during which participants responded to 32 images (128 evaluation points). All evaluation points belonging to the same image were assigned to the same group of participants to en-

sure within-image consistency in perceptual judgments. After data collection, we excluded outlier participants whose depth estimates showed low Pearson correlation with the group mean. The effective number of responses per image after screening was 17.88 on average (range: 14–24, see Appendix A.2). The study protocol was approved by the authors’ institutional review board, and the experiment was conducted in accordance with the Declaration of Helsinki.

3.2. Target DNNs: 69 monocular depth estimators

To systematically compare DNNs with human estimates, we assembled a diverse set of 69 monocular depth estimators encompassing a wide range of architectures, training strategies, datasets, and output formats (full-list is available in Appendix A.3). Note that we exclusively target models trained to minimize the discrepancy with ground-truth physical depth, allowing us to investigate human similarity as an emergent property of this optimization.

In terms of training strategies, we included supervised models, trained on RGB images and the corresponding physical depth maps as the ground-truth signals, and self-supervised models, trained on image sequences or stereo pairs by leveraging disparity and camera pose cues instead of explicit depth labels. At inference time, the latter infer depth from a single RGB image, enabling monocular estimation without multiple frames. We also incorporated hybrid approaches that combine supervised and self-supervised components—such as ‘hybrid (disparity)’ models that integrate stereo disparity within a supervised framework [49], and ‘hybrid (semantics)’ models that leverage semantic representations obtained from large-scale contrastive pretraining [40]. Additionally, a subset of generative models based on recent diffusion techniques [31] was evaluated. Regarding model architectures, our model set included CNNs, Transformers, CNN-Transformer hybrids, and diffusion-based architectures.

Regarding training data variations, our evaluation employed models trained on both the outdoor KITTI benchmark and the indoor NYU Depth V2 benchmark [46], while also including models trained on other datasets—covering additional indoor datasets (Bonn [41] and TUM [47]), an outdoor dataset (DDAD [16]), and several large-scale mixed-domain datasets. Moreover, some models (e.g., MiDaS [44] and DINOv2 [40]) were first pretrained on a wide variety of heterogeneous datasets, with some subsequently being fine-tuned on domain-specific benchmarks such as KITTI or NYU. These mixed-training and fine-tuning strategies are explicitly categorized as “KITTI + multiple datasets” or “NYU + multiple datasets” in our subsequent analyses.

3.3. Similarity analysis based on estimation errors

To quantify the similarity between human and DNN depth estimation errors, we performed a partial correlation analysis based on a random half-split human data. Specifically, we first randomly partitioned the human observers into two independent groups and computed their mean depth estimates for each evaluation point. The human-human similarity was defined as the partial correlation between the mean estimates of these two groups, providing a measure of the internal consistency of human perceptual biases. Similarly, the human-DNN similarity was defined as the partial correlation between the mean estimates of one randomly selected human group and the DNN depth estimates. This procedure was repeated 1,000 times with different random splits, and the expected values across iterations were taken as the final human-human and human-DNN similarity scores. This analysis quantifies the shared variance between human and model error patterns while controlling for variance explained by the physical ground truth (i.e., the correlation between their residuals after regressing out ground truth).

Because the 69 MDE models differ in output representations (e.g., absolute depth, disparity, or scale-shift invariant depth), we adopted a two-stage comparison framework. In the first stage, we directly compared human estimates with 36 DNNs that output absolute depth. In the second stage, to ensure comparability across all 69 DNNs, we performed scale-recovered processing by linearly regressing each DNN’s output and the human (random half-split) data against the physical ground-truth depth, using the 16 evaluation points per image. This regression yielded metric-aligned “pseudo-absolute” depth estimates for all DNNs. Based on these aligned values, we computed a scale-shift-invariant RMSE as a standardized measure of model accuracy. Human-human and human-DNN partial correlations were recalculated using these scale-recovered estimates.

3.4. Affine decomposition analysis

To gain a more granular understanding of the estimation errors, we employ an affine decomposition analysis, which disentangles systematic, per-image distortions into interpretable geometric components (scale, shift, shear, and residual). The choice of this model is well-founded. Monocular 3D reconstruction is an ill-posed problem with inherent affine ambiguities (e.g., the “bas-relief ambiguity” [2]). Consequently, to resolve this ambiguity, DNNs must implicitly learn priors from the training data, which often manifest as systematic estimation biases. Conveniently, a parallel finding exists in psychophysical research: human depth perception itself exhibits consistent, affine-like distortions, rather than being metrically accurate [25, 53]. This parallel makes affine analysis a particularly effective framework for comparing the systematic biases learned by DNNs against those intrinsic to the human visual system [27].

Specifically, for each image, we fitted an affine transformation to the 16 depth estimates of humans and DNNs, $z_{\text{est}}^{(i)}$ ($i = 1, \dots, 16$), from the ground truth depth, z_{GT} : $z_{\text{est}}^{(i)} \simeq a_z * z_{\text{GT}}^{(i)} + a_x * p_x^{(i)} + a_y * p_y^{(i)} + b$, where the four regression coefficients represent interpretable, per-image bias components: a_z (scale), b (shift), a_x (horizontal shear), and a_y (vertical shear). The pixel coordinates p_x and p_y were normalized to the range $[-1, 1]$, and a_z was constrained to be positive to ensure geometrical validity. This fitting procedure produced four affine coefficients and a residual component for each image, where the residual was defined as $z_{\text{res}} = z_{\text{pred}} - z_{\text{est}}$, with z_{pred} denoting the affine fitting’s prediction of z_{est} . Together, these parameters provided a detailed and interpretable decomposition of systematic depth estimation biases across humans and DNNs. We then quantified the alignment of these biases by computing the Pearson correlation between the series of coefficients and residuals from humans and those from each DNN across all images.

4. Results

For visualization, DNNs were color-coded into six categories according to the composition of their training datasets. DNNs trained exclusively on the KITTI dataset are shown in blue, while those fine-tuned on KITTI after pretraining on multiple datasets are shown in purple. Similarly, DNNs trained solely on the NYU dataset appear in red, and those fine-tuned on NYU following multi-dataset pretraining are shown in orange. DNNs trained on either a single dataset or a diverse mixture of datasets, both excluding KITTI and NYU, are shown in cyan and green, respectively. In addition, distinct marker shapes were used to distinguish variations in training strategies.

4.1. Model performance: RMSE and human similarity

We first evaluated DNN accuracy against the physical ground truth using RMSE, as shown in Figure 2A. For both absolute (left column) and scale-recovered data (right column), DNNs trained on in-distribution KITTI data (blue and purple) achieved the lowest errors, outperforming human observers. Models trained on the out-of-distribution NYU dataset performed substantially worse, confirming the advantage of in-distribution training.

We next assessed the similarity of DNN error patterns to those of humans. As a perceptual benchmark, we first confirmed a high degree of inter-personal consistency in human depth judgments, indicating the reliability of these measurements (Figure 2B). When compared against this human benchmark, all 36 DNNs that output absolute depth estimates exhibited positive correlations with human error patterns (left column), as measured by Pearson partial correlations. This suggests that models acquire human-like biases

even when trained solely on physical ground truth. Nevertheless, no DNN reached the high level of consistency observed between humans. A similar pattern was observed for scale-recovered depth estimations (Figure 2B, right column).

4.2. Trade-off relationships between model accuracy and human similarity

To dissect the interplay between metric accuracy and human similarity, we visualized their relationship using scatter plots (Figure 1, “Results”). For this analysis, the horizontal axis represents model accuracy quantified by scale-shift invariant RMSE (log scale). This metric is used for both absolute and scale-recovered models to ensure a fair comparison by normalizing for the inherent scale differences across training datasets. The vertical axis shows human similarity, measured as the partial correlation between human and DNN error patterns. In absolute data, human similarity did not systematically increase with accuracy; instead, it appeared to peak before slightly declining. In the scale-recovered data, this trend became more pronounced, forming a clear inverse-U relationship: DNNs with the highest metric accuracy tended to exhibit lower human-similarity. Interestingly, DNNs most similar to humans were those achieving roughly human-level accuracy.

To quantify the trade-off observed around human-level accuracy, we divided the DNNs into two groups using the human RMSE value as a boundary: human-superior group (with smaller RMSE than humans) and human-inferior group (with larger RMSE). Within each group, we computed the Pearson correlation (r) between log-RMSE (scale-shift invariant RMSE with log scale) and human similarity. For human-inferior DNNs, we found negative correlations (absolute: $r = -0.22$, $p = 0.38$, scale-recovered: $r = -0.56$, $p < 0.001$), showing that moderate improvements in accuracy were accompanied by stronger human alignment. In contrast, for human-superior DNNs, the correlation reversed (absolute: $r = 0.37$, $p = 0.14$; scale-recovered: $r = 0.69$, $p < 0.001$), revealing a trade-off effect—where further accuracy gains no longer led to greater human similarity and were instead associated with reduced alignment to human depth perception.

4.3. Trade-off relationships in affine coefficients and the residual error

To gain a more detailed understanding of the factors underlying human and DNN depth estimation errors, we conducted an affine decomposition of the per-image estimation errors. This analysis provides a structured framework for disentangling how different geometric components contribute to systematic deviations in depth estimation. Figure 3 presents this relationship, where model accuracy (scale-shift invariant RMSE) is plotted against human-DNN

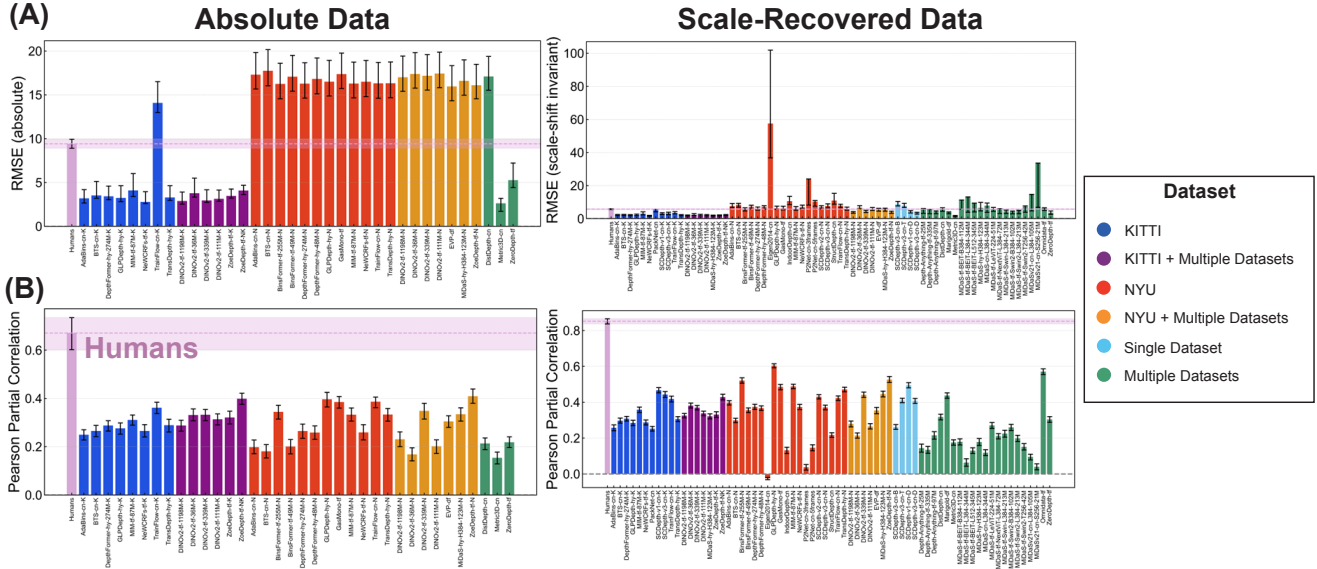


Figure 2. Comparison of human and DNN error profiles for absolute (left) and scale-recovered (right) data. (A) RMSE of raw errors against the physical ground-truth depth. (B) Pearson partial correlations used to quantify similarity between humans and DNNs.

correlations for each of the four affine coefficients and the residual error (see Appendix B.1 for a comparison of their average values).

When focusing on the relationship between model accuracy and human similarity, the inverse-U pattern became even more pronounced (Figure 3), as also confirmed by the quantitative analysis in Appendix B.2. This trade-off relationship was consistently observed across all decomposed affine components. Moreover, the rankings of DNNs in terms of human similarity were largely consistent across these components (see Appendix B.3), suggesting that shared human-like biases are expressed coherently across multiple geometric dimensions of depth estimation rather than being confined to isolated factors.

Most notably, we found that several DNNs with roughly human-level accuracy—despite being trained solely to reproduce physical depth—achieved human similarity scores comparable to those of human observers.

4.4. Effects of dataset and backbone architecture

Beyond accuracy, we also examined how training datasets and backbone architectures affect human-DNN similarity. Our analysis revealed several nuanced trends rather than a single decisive factor (see Appendix B.4 for a detailed comparison). Overall, models trained on the NYU dataset tended to exhibit higher human similarity, though this was not universal; in some model families, the KITTI-trained variant performed better. Regarding backbone architectures, a comparison within the KITTI, NYU, and MiDaS model family, all trained on the same dataset, suggested

that Transformer-based models showed a slight advantage over CNNs, with mid-sized models often achieving the highest similarity. Finally, we observed no clear evidence that specific training strategies, such as generative or self-supervised methods, consistently produced more human-like behavior.

4.5. Qualitative visualization: depth estimation biases in humans and DNNs

To qualitatively investigate the differences in depth estimation strategies between humans and high-performing DNNs, we visualized their respective depth estimations overlaid on the KITTI images. Figure 4 illustrates a comparison between human estimates and those produced by two representative DNNs: NeWCRFs-K, the state-of-the-art (SOTA) model according to our scale-shift invariant RMSE benchmark, and ZoeDepth-NK, which stands out as one of the most human-like models in our evaluation. It was chosen for its high similarity score combined with an output scale compatible with the KITTI scenes, making it ideal for qualitative visualization. The present images were selected to highlight perceptually biased cases—specifically, scenes characterized by distinctive horizontal (a_x) and vertical (a_y) shear coefficients in the human data. A broader selection of examples is provided in the Appendix B.5.

The visualizations reveal that both humans and the human-like DNN tend to estimate more points as being farther away than the ground truth, compared with the SOTA model. This general overestimation is particularly pronounced for vertical structures such as walls, trees, and ve-

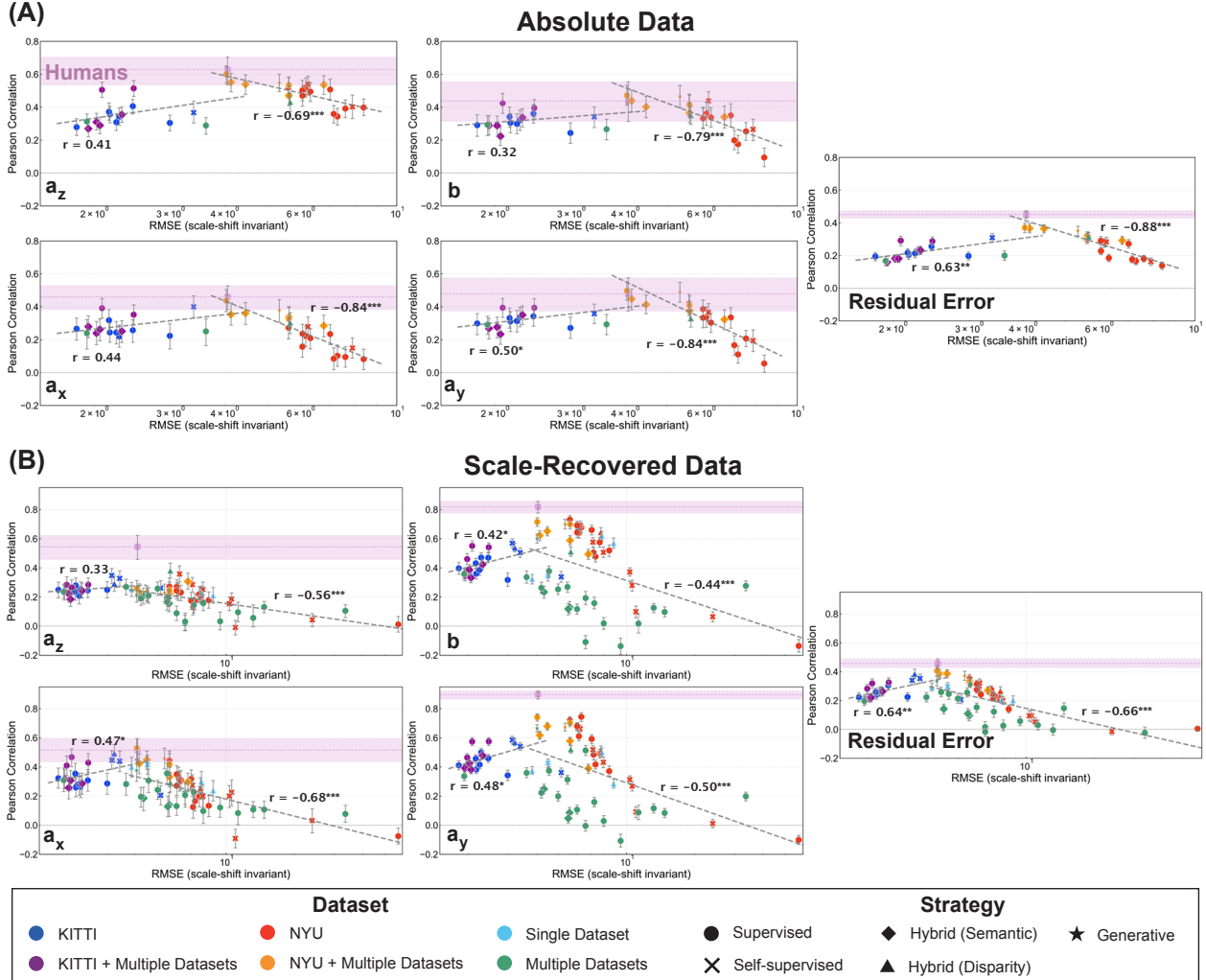


Figure 3. Scatter plots showing the relationship between model accuracy, quantified by scale-shift invariant RMSE, and human similarity for different components of the affine model. The analysis is presented separately for (A) 36 models that predict absolute depth values and (B) 69 models that predict scale-invariant depth (* : $p < 0.01$, ** : $p < 0.01$, and *** : $p < 0.001$).

hicles, whereas distances along the horizontal ground plane are estimated with greater accuracy. These error patterns indicate a systematic distortion in human-like spatial representation relative to the physical ground truth. The pronounced horizontal shear coefficients (a_x) observed in the human data likely reflect the asymmetric geometry of the KITTI scenes—such as oblique walls and roadside structures.

In contrast, for distance regions near the vanishing point, all three estimators—human, human-like, and SOTA—consistently underestimate depth. This tendency aligns with the well-documented depth compression effect in human perception [54, 55]. The presence of a similar bias in the DNN outputs suggests that they internalize statistical regularities from the training data that result in depth compression.

This shared characteristic likely contributes to the positive partial correlation frequently observed between human and DNN depth estimates.

5. Discussion

Our results reveal a clear trade-off between physical estimation accuracy and similarity to human estimates in the monocular depth estimation. This trade-off persists not only in overall error patterns but also across individual components derived from the affine decomposition analysis. Such finding parallel observations in object recognition research, where higher ImageNet accuracy often coincides with reduced human-likeness in perceptual metrics [9, 19, 29].

Interestingly, our KITTI-based analysis reveals a clear



Figure 4. Comparison of human and DNN depth estimation biases, illustrated with examples of characteristic horizontal (a_x) and vertical (a_y) shear patterns in human depth estimates. The top two rows show images with the largest positive and negative a_x values (6.67 and -6.55), while the bottom two rows show depict images with the minimum and maximum a_y values (-5.54 and -37.7).

inverse-U relationship, a pattern that was not distinctly observed in previous work adopting a similar human-centric approach on the NYU dataset [27]. We attribute the emergence of this distinct trade-off to KITTI’s unique statistical regularities. Unlike the diverse layouts and camera poses in NYU, the KITTI dataset is highly homogeneous, captured from a vehicle with a stable road-sky configuration. This homogeneity may encourage DNNs to adopt shortcut strategies tuned to its rigid geometry, causing them to diverge from the more flexible, context-driven priors characteristic of human vision.

This statistical homogeneity is not just compositional but also optical. KITTI’s fixed wide-angle FOV introduces a systematic geometric distortion, as wide-angle views are known to make objects appear farther in human perception [26]. DNNs optimized on KITTI may thus overfit to this unnatural spatial representation, diverging from human-like strategies. This aligns with our finding that NYU-tuned models tend to show higher human similarity, likely benefiting from more naturalistic visual statistics.

Our study underscores that progress in depth estimation cannot be fully captured by improvements in metric accuracy alone. Echoing recent calls for richer, multidimensional evaluation frameworks [56], evaluating how models align—or diverge—from human perceptual organization provides an additional lens for understanding their generalization and interpretability. Incorporating human-likeness as a complementary evaluation axis would uncover additional, perceptually grounded aspects of model behavior in monocular depth estimation that would otherwise remain

unrecognized.

Limitations and future work: Our study is limited by the scope of the datasets and our sparse data sampling, underscoring the need for evaluation on more diverse conditions with denser data. Beyond this, our work raises fundamental questions for future research. It is not yet empirically established whether increasing human similarity actually improves out-of-distribution robustness. This prompts a crucial follow-up question: is the accuracy/human-likeness trade-off an inherent cost for robust perception, or can models be developed that surpass human capabilities in both metric accuracy and robust generalization? Answering this is key to determining whether the path to advanced 3D vision requires emulating the human perceptual system or forging a fundamentally new one.

Possible social impact: While our human-centric evaluation aims to improve AI safety and interpretability, a model that faithfully emulates human vision could also reproduce its inherent perceptual biases, such as depth compression at far distances. This creates a risk of unintentionally embedding these biases into automated decisions or enabling the design of manipulative content that exploits the predictable ways humans perceive the world.

6. Conclusions

This study examined the relationship between model accuracy and human-like behavior in monocular depth estimation. By systematically comparing 69 diverse MDE models against human depth estimates on the KITTI dataset,

we found a trade-off between metric accuracy and human similarity: as DNNs achieved higher accuracy, their error patterns diverged from human depth estimates. This divergence was distinct in affine coefficients and residual components from our affine decomposition analysis, indicating that the most accurate models rely on estimation strategies that differ fundamentally from human depth computation. These findings demonstrate that higher metric accuracy does not necessarily yield more human-like estimation behavior, underscoring the need for evaluation frameworks with human-centered benchmarks to better capture perceptual alignment and robustness in 3D vision models.

References

- [1] Jinwoo Bae, Kyumin Hwang, and Sunghoon Im. A study on the generality of neural network structures for monocular depth estimation. *IEEE Transactions on Pattern Analysis and Machine Intelligence*, 46(4):2224–2238, 2023. 1, 2
- [2] Peter N Belhumeur, David J Kriegman, and Alan L Yuille. The bas-relief ambiguity. *International journal of computer vision*, 35(1):33–44, 1999. 4
- [3] Shariq Farooq Bhat, Ibraheem Alhashim, and Peter Wonka. Adabins: Depth estimation using adaptive bins. In *Proceedings of the IEEE/CVF Conference on Computer Vision and Pattern Recognition*, pages 4009–4018, 2021. 13, 17
- [4] Shariq Farooq Bhat, Reiner Birkel, Diana Wofk, Peter Wonka, and Matthias Müller. Zoedepth: Zero-shot transfer by combining relative and metric depth. *arXiv preprint arXiv:2302.12288*, 2023. 13, 14, 17
- [5] Jia-Wang Bian, Huangying Zhan, Naiyan Wang, Tat-Jun Chin, Chunhua Shen, and Ian Reid. Auto-rectify network for unsupervised indoor depth estimation. *IEEE Transactions on Pattern Analysis and Machine Intelligence*, 44(12):9802–9813, 2021. 13
- [6] Jia-Wang Bian, Huangying Zhan, Naiyan Wang, Zhichao Li, Le Zhang, Chunhua Shen, Ming-Ming Cheng, and Ian Reid. Unsupervised scale-consistent depth learning from video. *International Journal of Computer Vision*, 129(9):2548–2564, 2021. 13
- [7] Reiner Birkel, Diana Wofk, and Matthias Müller. MiDaS v3.1 – a model zoo for robust monocular relative depth estimation. *arXiv preprint arXiv:2307.14460*, 2023. 1, 13
- [8] Weifeng Chen, Zhao Fu, Dawei Yang, and Jia Deng. Single-image depth perception in the wild. *Advances in Neural Information Processing Systems*, 29, 2016. 1, 3
- [9] Mostafa Dehghani, Josip Djolonga, Basil Mustafa, Piotr Padlewski, Jonathan Heek, Justin Gilmer, Andreas Peter Steiner, Mathilde Caron, Robert Geirhos, Ibrahim Alabdulmohsin, et al. Scaling Vision Transformers to 22 billion parameters. In *International Conference on Machine Learning*, pages 7480–7512, 2023. 1, 7
- [10] Ainaz Eftekhari, Alexander Sax, Jitendra Malik, and Amir Zamir. Omnidata: A scalable pipeline for making multi-task mid-level vision datasets from 3d scans. In *Proceedings of the IEEE/CVF International Conference on Computer Vision*, pages 10786–10796, 2021. 13
- [11] David Eigen, Christian Puhrsch, and Rob Fergus. Depth map prediction from a single image using a multi-scale deep network. *Advances in Neural Information Processing Systems*, 27, 2014. 1, 2, 13
- [12] Logan Engstrom, Andrew Ilyas, Shibani Santurkar, Dimitris Tsipras, Brandon Tran, and Aleksander Madry. Adversarial robustness as a prior for learned representations. *arXiv preprint arXiv:1906.00945*, 2019. 1
- [13] Chao Fan, Zhenyu Yin, Yue Li, and Feiqing Zhang. Deeper into self-supervised monocular indoor depth estimation. *arXiv preprint arXiv:2312.01283*, 2023. 13
- [14] Robert Geirhos, Patricia Rubisch, Claudio Michaelis, Matthias Bethge, Felix A Wichmann, and Wieland Brendel. ImageNet-trained CNNs are biased towards texture; increasing shape bias improves accuracy and robustness. In *International Conference on Learning Representations*, 2018. 1
- [15] Robert Geirhos, Carlos RM Temme, Jonas Rauber, Heiko H Schütt, Matthias Bethge, and Felix A Wichmann. Generalisation in humans and deep neural networks. *Advances in Neural Information Processing Systems*, 31, 2018. 1
- [16] Vitor Guizilini, Rares Ambrus, Sudeep Pillai, Allan Ravesantos, and Adrien Gaidon. 3D packing for self-supervised monocular depth estimation. In *Proceedings of the IEEE/CVF Conference on Computer Vision and Pattern Recognition*, pages 2485–2494, 2020. 4, 13, 14
- [17] Vitor Guizilini, Igor Vasiljevic, Dian Chen, Rares Ambrus, and Adrien Gaidon. Towards zero-shot scale-aware monocular depth estimation. In *Proceedings of the IEEE/CVF International Conference on Computer Vision*, pages 9233–9243, 2023. 13
- [18] Martin N Hebart, Charles Y Zheng, Francisco Pereira, and Chris I Baker. Revealing the multidimensional mental representations of natural objects underlying human similarity judgements. *Nature Human Behaviour*, 4(11):1173–1185, 2020. 1
- [19] Pablo Hernández-Cámara, Jose Manuel Jaén-Lorites, Jorge Vila-Tomás, Valero Laparra, and Jesus Malo. Do Vision Transformers see like humans? Evaluating their perceptual alignment. *arXiv preprint arXiv:2508.09850*, 2025. 1, 7
- [20] Lukas S Huber, Fred W Mast, and Felix A Wichmann. Immediate generalisation in humans but a generalisation lag in deep neural networks—evidence for representational divergence? *arXiv preprint arXiv:2402.09303*, 2024. 1
- [21] Johan Hulleman and Glyn W Humphreys. A new cue to figure-ground coding: Top-bottom polarity. *Vision Research*, 44(24):2779–2791, 2004. 14
- [22] Bingxin Ke, Anton Obukhov, Shengyu Huang, Nando Metzger, Rodrigo Caye Daudt, and Konrad Schindler. Repurposing diffusion-based image generators for monocular depth estimation. In *Proceedings of the IEEE/CVF Conference on Computer Vision and Pattern Recognition*, pages 9492–9502, 2024. 1, 12, 13
- [23] Doyeon Kim, Woonghyun Ka, Pyungwhan Ahn, Donggyu Joo, Sehwan Chun, and Junmo Kim. Global-local path networks for monocular depth estimation with vertical cutdepth. *arXiv preprint arXiv:2201.07436*, 2022. 13, 17

- [24] Alexander Kirillov, Eric Mintun, Nikhila Ravi, Hanzi Mao, Chloe Rolland, Laura Gustafson, Tete Xiao, Spencer Whitehead, Alexander C. Berg, Wan-Yen Lo, Piotr Dollár, and Ross Girshick. Segment anything. *arXiv:2304.02643*, 2023. 12
- [25] Jan J Koenderink, Andrea J van Doorn, Astrid M L Kap-pers, and James T Todd. Ambiguity and the ‘mental eye’ in pictorial relief. *Perception*, 30(4):431–448, 2001. PMID: 11383191. 3, 4
- [26] Robert N Kraft and Jeffrey S Green. Distance perception as a function of photographic area of view. *Perception & Psychophysics*, 45(5):459–466, 1989. 8, 14
- [27] Yuki Kubota and Taiki Fukiage. Human-like monocular depth biases in deep neural networks. *PLOS Computational Biology*, 21(8):e1013020, 2025. 1, 2, 3, 4, 8
- [28] Yuki Kubota, Ryota Mima, Takahiro Kawabe, Taiki Fukiage, and Masahiko Inami. Motion-driven enhancement of a lower region cue in depth perception. *Journal of Illusion*, 3, 2022. 14
- [29] Manoj Kumar, Neil Houlsby, Nal Kalchbrenner, and Ekin D Cubuk. Do better ImageNet classifiers assess perceptual similarity better? *arXiv preprint arXiv:2203.04946*, 2022. 1, 7
- [30] Michael S Landy, Laurence T Maloney, Elizabeth B Johnston, and Mark Young. Measurement and modeling of depth cue combination: in defense of weak fusion. *Vision Research*, 35(3):389–412, 1995. 3
- [31] Mykola Lavreniuk, Shariq Farooq Bhat, Matthias Müller, and Peter Wonka. EVP: Enhanced visual perception using inverse multi-attentive feature refinement and regularized image-text alignment. *arXiv preprint arXiv:2312.08548*, 2023. 1, 4, 12, 13
- [32] Hyunmin Lee and Jaesik Park. Instance-wise occlusion and depth orders in natural scenes. In *Proceedings of the IEEE/CVF Conference on Computer Vision and Pattern Recognition*, pages 21210–21221, 2022. 1, 3
- [33] Jin Han Lee, Myung-Kyu Han, Dong Wook Ko, and Il Hong Suh. From big to small: Multi-scale local planar guidance for monocular depth estimation. *arXiv preprint arXiv:1907.10326*, 2019. 13, 17
- [34] Boying Li, Yuan Huang, Zeyu Liu, Danping Zou, and Wenxian Yu. Structdepth: Leveraging the structural regularities for self-supervised indoor depth estimation. In *Proceedings of the IEEE/CVF International Conference on Computer Vision*, pages 12663–12673, 2021. 13
- [35] Zhenyu Li, Zehui Chen, Xianming Liu, and Junjun Jiang. DepthFormer: Exploiting long-range correlation and local information for accurate monocular depth estimation. *Machine Intelligence Research*, 20:837–854, 2023. 1, 13, 17
- [36] Zhenyu Li, Xuyang Wang, Xianming Liu, and Junjun Jiang. Binsformer: Revisiting adaptive bins for monocular depth estimation. *IEEE Transactions on Image Processing*, 33: 3964–3976, 2024. 13
- [37] Chenxi Liao, Masataka Sawayama, and Bei Xiao. Unsupervised learning reveals interpretable latent representations for translucency perception. *PLOS Computational Biology*, 19(2):e1010878, 2023. 1
- [38] Paul Linton, Michael J Morgan, Jenny C A Read, Dhanraj Vishwanath, Sarah H Creem-Regehr, and Fulvio Domini. New approaches to 3D vision. *Philosophical Transactions of the Royal Society B*, 378:20210443, 2023. 3
- [39] Lukas Muttenthaler, Lorenz Linhardt, Jonas Dippel, Robert A Vandermeulen, Katherine Hermann, Andrew Lampinen, and Simon Kornblith. Improving neural network representations using human similarity judgments. *Advances in Neural Information Processing Systems*, 36:50978–51007, 2023. 1
- [40] Maxime Oquab, Timothée Darcet, Theo Moutakanni, Huy V. Vo, Marc Szafraniec, Vasil Khalidov, Pierre Fernandez, Daniel Haziza, Francisco Massa, Alaaeldin El-Nouby, Russell Howes, Po-Yao Huang, Hu Xu, Vasu Sharma, Shang-Wen Li, Wojciech Galuba, Mike Rabbat, Mido Assran, Nicolas Ballas, Gabriel Synnaeve, Ishan Misra, Herve Jegou, Julien Mairal, Patrick Labatut, Armand Joulin, and Piotr Bojanowski. DINOv2: Learning robust visual features without supervision. *arXiv:2304.07193*, 2023. 1, 4, 12, 13, 17
- [41] Emanuele Palazzolo, Jens Behley, Philipp Lottes, Philippe Giguere, and Cyrill Stachniss. ReFusion: 3D reconstruction in dynamic environments for RGB-D cameras exploiting residuals. In *IEEE/RSJ International Conference on Intelligent Robots and Systems*, pages 7855–7862. IEEE, 2019. 4, 12
- [42] Konrad Eugen Prokott, Hideki Tamura, and Roland W Fleming. Gloss perception: Searching for a deep neural network that behaves like humans. *Journal of Vision*, 21(12):14–14, 2021. 1
- [43] René Ranftl, Katrin Lasinger, David Hafner, Konrad Schindler, and Vladlen Koltun. Towards robust monocular depth estimation: Mixing datasets for zero-shot cross-dataset transfer. *IEEE Transactions on Pattern Analysis and Machine Intelligence*, 44(3):1623–1637, 2020. 2, 13, 14
- [44] René Ranftl, Alexey Bochkovskiy, and Vladlen Koltun. Vision transformers for dense prediction. In *Proceedings of the IEEE/CVF International Conference on Computer Vision*, pages 12179–12188, 2021. 1, 4, 13, 14, 17
- [45] Robin Rombach, Andreas Blattmann, Dominik Lorenz, Patrick Esser, and Björn Ommer. High-resolution image synthesis with latent diffusion models. In *Proceedings of the IEEE/CVF conference on computer vision and pattern recognition*, pages 10684–10695. IEEE, 2022. 12
- [46] Nathan Silberman, Derek Hoiem, Pushmeet Kohli, and Rob Fergus. Indoor segmentation and support inference from RGBD images. In *Proceedings of the European Conference on Computer Vision*, pages 746–760. Springer, 2012. 2, 4, 12
- [47] Jürgen Sturm, Nikolas Engelhard, Felix Endres, Wolfram Burgard, and Daniel Cremers. A benchmark for the evaluation of RGB-D SLAM systems. In *IEEE/RSJ International Conference on Intelligent Robots and Systems*, pages 573–580. IEEE, 2012. 4, 12
- [48] Ilia Sucholutsky, Lukas Muttenthaler, Adrian Weller, Andi Peng, Andreea Bobu, Been Kim, Bradley C Love, Erin Grant, Iris Groen, Jascha Achterberg, et al. Getting aligned on representational alignment. *arXiv preprint arXiv:2310.13018*, 2023. 1
- [49] Libo Sun, Jia-Wang Bian, Huangying Zhan, Wei Yin, Ian Reid, and Chunhua Shen. SC-Depthv3: Robust self-

- supervised monocular depth estimation for dynamic scenes. *IEEE Transactions on Pattern Analysis and Machine Intelligence*, 2023. 1, 4, 12, 13, 17
- [50] Jonas Uhrig, Nick Schneider, Lukas Schneider, Uwe Franke, Thomas Brox, and Andreas Geiger. Sparsity invariant CNNs. In *International Conference on 3D Vision*, pages 11–20. IEEE, 2017. 2, 3, 12
- [51] Andrea J van Doorn, Johan Wagemans, Huib de Ridder, and Jan J Koenderink. Space perception in pictures. In *SPIE Human Vision and Electronic Imaging XVI*, pages 423–430. SPIE, 2011. 3
- [52] Shaun P Vecera, Edward K Vogel, and Geoffrey F Woodman. Lower region: A new cue for figure-ground assignment. *Journal of Experimental Psychology: General*, 131(2):194–205, 2002. 14
- [53] Johan Wagemans, Andrea J van Doorn, and Jan J Koenderink. Measuring 3D point configurations in pictorial space. *i-Perception*, 2(1):77–111, 2011. 3, 4
- [54] Mark Wagner. The metric of visual space. *Perception & Psychophysics*, 38:483–495, 1985. 7
- [55] Mark Wagner and Anthony J. Gambino. Variations in the anisotropy and affine structure of visual space: A geometry of visibles with a third dimension. *Topoi*, 35(2):583–598, 2016. 3, 7
- [56] Felix A Wichmann and Robert Geirhos. Are deep neural networks adequate behavioral models of human visual perception? *Annual Review of Vision Science*, 9(1):501–524, 2023. 1, 8
- [57] Cho-Ying Wu, Jialiang Wang, Michael Hall, Ulrich Neumann, and Shuochen Su. Toward practical monocular indoor depth estimation. In *Proceedings of the IEEE/CVF Conference on Computer Vision and Pattern Recognition*, pages 3814–3824, 2022. 12, 13
- [58] Zhenda Xie, Zigang Geng, Jingcheng Hu, Zheng Zhang, Han Hu, and Yue Cao. Revealing the dark secrets of masked image modeling. In *Proceedings of the IEEE/CVF Conference on Computer Vision and Pattern Recognition*, pages 14475–14485, 2023. 13
- [59] Daniel LK Yamins, Ha Hong, Charles F Cadieu, Ethan A Solomon, Darren Seibert, and James J DiCarlo. Performance-optimized hierarchical models predict neural responses in higher visual cortex. *Proceedings of the National Academy of Sciences*, 111(23):8619–8624, 2014. 1
- [60] Guanglei Yang, Hao Tang, Mingli Ding, Nicu Sebe, and Elisa Ricci. Transformer-based attention networks for continuous pixel-wise prediction. In *Proceedings of the IEEE/CVF International Conference on Computer vision*, pages 16269–16279, 2021. 13, 17
- [61] Lihe Yang, Bingyi Kang, Zilong Huang, Xiaogang Xu, Jiashi Feng, and Hengshuang Zhao. Depth Anything: Unleashing the power of large-scale unlabeled data. In *Proceedings of IEEE/CVF Conference on Computer Vision and Pattern Recognition*, pages 10371–10381, 2024. 2, 12, 13, 14
- [62] Yung-Hao Yang, Taiki Fukiage, Zitang Sun, and Shin’ya Nishida. Psychophysical measurement of perceived motion flow of naturalistic scenes. *iScience*, 26(12):108307, 2023. 1
- [63] Yung-Hao Yang, Zitang Sun, Taiki Fukiage, and Shin’ya Nishida. HuPerFlow: A comprehensive benchmark for human vs. machine motion estimation comparison. In *Proceedings of the Computer Vision and Pattern Recognition Conference*, pages 22799–22808, 2025. 1
- [64] Zhiyong Yang and Dale Purves. A statistical explanation of visual space. *Nature Neuroscience*, 6:632–640, 2003. 3
- [65] Wei Yin, Chi Zhang, Hao Chen, Zhipeng Cai, Gang Yu, Kaixuan Wang, Xiaozhi Chen, and Chunhua Shen. Metric3d: Towards zero-shot metric 3d prediction from a single image. In *Proceedings of the IEEE/CVF International Conference on Computer Vision*, pages 9043–9053, 2023. 13, 14
- [66] Zehao Yu, Lei Jin, and Shenghua Gao. P²net: Patch-match and plane-regularization for unsupervised indoor depth estimation. In *European Conference on Computer Vision*, pages 206–222. Springer, 2020. 13
- [67] Weihao Yuan, Xiaodong Gu, Zuozhuo Dai, Siyu Zhu, and Ping Tan. NeW CRFs: Neural window fully-connected CRFs for monocular depth estimation. In *Proceedings of the IEEE/CVF Conference on Computer Vision and Pattern Recognition*, pages 3906–3915, 2022. 1, 13, 17
- [68] Chaoqiang Zhao, Matteo Poggi, Fabio Tosi, Lei Zhou, Qiyu Sun, Yang Tang, and Stefano Mattoccia. GasMono: Geometry-aided self-supervised monocular depth estimation for indoor scenes. In *Proceedings of the IEEE/CVF International Conference on Computer Vision*, pages 16209–16220, 2023. 1, 13
- [69] Wang Zhao, Shaohui Liu, Yezhi Shu, and Yong-Jin Liu. Towards better generalization: Joint depth-pose learning without posenet. In *Proceedings of the IEEE/CVF Conference on Computer Vision and Pattern Recognition*, pages 9151–9161, 2020. 13
- [70] Daniel Zoran, Phillip Isola, Dilip Krishnan, and William T. Freeman. Learning ordinal relationships for mid-level vision. *Proceedings of the IEEE International Conference on Computer Vision*, 2015. 3

A. Supplemental Methods

All human data and analysis code will be officially released in a public repository upon publication. They are provided in the `script` directory within the supplemental materials as temporary files until the public release.

A.1. Per-image evaluation point sampling

For each of the 328 evaluation images, we selected four groups of four evaluation points (sixteen points per image) following three spatial constraints designed to ensure the reliability of the evaluation points: (A) Points within each group were separated by at least 20 pixels in both vertical and horizontal directions. (B) All points were located more than 20 pixels away from image borders to avoid boundary-related artifacts. (C) To prevent ambiguity near object edges, each point was placed at least 5 pixels away from segmentation boundaries estimated by the Segment Anything Model (SAM) [24].

Candidate points were selected through an iterative sampling procedure. A randomly selected point p_i was compared with all previously chosen points $[p_0, \dots, p_{i-1}]$ to verify that it satisfied the three spatial constraints. If any condition was violated, nearby pixels within the same segmentation region were explored as alternative candidates. This local search strategy reduced the oversampling of large homogeneous areas such as roads or walls. When no valid candidate could be found within a given segment, the selection process was reinitialized until a complete set of sixteen valid points was obtained. The final point sets were subsequently used to collect absolute depth estimations from human participants.

A.2. Human data collection procedure

Participants were recruited via an online crowdsourcing platform, including adults in their 20s to 40s (890 participants). All observations were made binocularly. Before starting the experiment, participants were instructed to disable dark or night mode on their browsers and to view the stimuli in full-screen mode. To standardize the physical size of stimuli across different display devices, participants adjusted an on-screen rectangle to match the size of a credit card held in their hand. This calibration ensured consistent stimulus scaling based on individual screen pixel density, resulting in an image size of 18.6 cm \times 5.63 cm. Participants were also instructed to maintain a consistent viewing distance of 60 cm, which resulted in a stimulus visual angle of approximately $17.6^\circ \times 5.37^\circ$. Although our online setup did not allow for detailed control of viewing conditions or individual visual acuity, averaging responses across a large sample reduced potential variability from such uncontrolled factors.

Prior to the main trials, participants completed five practice trials with feedback to ensure task comprehension. During the experiment, they were presented with stimuli containing four labeled target points (A–D) and were asked to estimate the distance of each point from their viewpoint, imagining themselves positioned at the camera location. For reflective or transparent surfaces (e.g., mirrors, glass), participants reported the perceived distance to the physical surface itself. Each participant completed 32 randomized trials, and every stimulus set was evaluated by at least 20 individuals.

To maintain high data quality, we excluded participants whose responses showed low reliability. Reliability was evaluated using the Pearson correlation between each participant’s judgments and the group median responses. Because the proportion of unreliable participants could vary across stimulus sets, we used a two-stage procedure to assess response reliability. First, we computed the Pearson correlation between an individual’s responses and the average responses within each group of participants who viewed the same stimuli. Second, all correlation values were pooled across participants, and the interquartile range (IQR) of this overall distribution was used to determine a global cutoff for exclusion. Participants whose reliability scores fell more than $1.5 \times \text{IQR}$ below the central distribution were classified as outliers and removed from further analyses. Finally, we yielded a final dataset of 733 valid participants (average: 17.88, range: 14–24) for the absolute depth judgment task.

A.3. Target DNN models

Table A1 summarizes the 69 monocular depth estimators adopted in this study. The collection includes DNNs trained with diverse strategies—supervised, self-supervised, hybrid, and generative—, backbone architectures (CNN-, Transformer-, hybrid-, and diffusion-based), datasets, and parameter sizes. Supervised approaches employ ground-truth depth supervision, while self-supervised models learn from photometric consistency across stereo or monocular sequences. Hybrid methods integrate both paradigms: ‘hybrid (disparity)’ models, such as DistDepth [57] and SCDepth-v3 [49], combine teacher-student supervision with disparity-based self-training; ‘hybrid (semantic)’ models, including Depth-Anything [61] and DINOv2 [40], leverage semantic features from large-scale contrastive pretraining. Generative models, such as EVP [31] and Marigold [22], incorporate diffusion-based representations via Stable Diffusion [45] coupled with supervised decoders for depth estimations.

Our evaluation covers DNNs trained not only on NYU [46] and KITTI [50] but also on broader datasets to examine generalization across domains. These include indoor datasets such as Bonn [41] and TUM [47], as well as outdoor datasets like

Table A1. Target 69 DNN model list. The models outputs were categorized based on the type of depth information provided: absolute depth (no symbol), relative depth (indicated by †), and disparity (indicated by ‡). Full version of this table is available as the `model_list.csv` file.

Models	Strategy	Backbone	Dataset			Size
			KITTI	NYU	Others	
AdaBins-cn-K [3]	supervised	CNN	✓	-	-	78,257,238
AdaBins-cn-N [3]	supervised	CNN	-	✓	-	78,257,238
BinsFormer-tf-49M-N [36]	supervised	Transformer	-	✓	-	49,231,191
BinsFormer-tf-255M-N [36]	supervised	Transformer	-	✓	-	254,625,329
BTS-cn-K [33]	supervised	CNN	✓	-	-	47,481,969
BTS-cn-N [33]	supervised	CNN	-	✓	-	47,481,969
Depth-Anything-tf-25M [61]†	hybrid (semantic)	Transformer	-	-	14 datasets	24,785,089
Depth-Anything-tf-97M [61]†	hybrid (semantic)	Transformer	-	-	14 datasets	97,470,785
Depth-Anything-tf-335M [61]†	hybrid (semantic)	Transformer	-	-	14 datasets	335,315,649
DepthFormer-hy-48M-N [35]	supervised	hybrid	-	✓	-	47,612,029
DepthFormer-hy-274M-K [35]	supervised	hybrid	✓	-	-	273,732,631
DepthFormer-hy-274M-N [35]	supervised	hybrid	-	✓	-	273,732,631
DINOv2-tf-36M-K [40]	hybrid (semantic)	Transformer	✓	-	1.2B data	36,017,953
DINOv2-tf-36M-N [40]	hybrid (semantic)	Transformer	-	✓	1.2B data	36,017,953
DINOv2-tf-111M-K [40]	hybrid (semantic)	Transformer	✓	-	1.2B data	110,774,401
DINOv2-tf-111M-N [40]	hybrid (semantic)	Transformer	-	✓	1.2B data	110,774,401
DINOv2-tf-339M-K [40]	hybrid (semantic)	Transformer	✓	-	1.2B data	338,558,657
DINOv2-tf-339M-N [40]	hybrid (semantic)	Transformer	-	✓	1.2B data	338,558,657
DINOv2-tf-1198M-K [40]	hybrid (semantic)	Transformer	✓	-	1.2B data	1,198,281,537
DINOv2-tf-1198M-N [40]	hybrid (semantic)	Transformer	-	✓	1.2B data	1,198,281,537
DistDepth-cn [57]	hybrid (disparity)	CNN	-	-	3 datasets	69,206,908
Eigen2014-cn [11]†	supervised	CNN	-	✓	-	240,833,218
EVP-df [31]	generative	Diffusion	-	✓	LAION-5B	933,814,544
GasMono-tf [68]	self-supervised	Transformer	-	✓	-	28,000,697
GLPDepth-hy-K [23]	supervised	hybrid	✓	-	-	61,220,903
GLPDepth-hy-N [23]	supervised	hybrid	-	✓	-	61,220,903
IndoorDepth-cn [13]†	self-supervised	CNN	-	✓	-	14,840,507
Marigold-df [22]†	generative	Diffusion	-	-	Hypersim, Virtual KITTI	1,289,963,947
Metric3D-cn [65]	supervised	CNN	-	-	11 datasets	203,243,090
MiDaS-tf-BEiT-B384-112M [7]‡	supervised	Transformer	-	-	10 datasets	111,531,689
MiDaS-tf-BEiT-L384-344M [7]‡	supervised	Transformer	-	-	10 datasets	344,338,601
MiDaS-tf-BEiT-L512-345M [7]‡	supervised	Transformer	-	-	10 datasets	345,014,441
MiDaS-tf-LeViT-224-51M [7]‡	supervised	Transformer	-	-	10 datasets	50,630,837
MiDaS-tf-NextViT-L384-72M [7]‡	supervised	Transformer	-	-	10 datasets	72,260,713
MiDaS-tf-Swin-L384-213M [7]‡	supervised	Transformer	-	-	10 datasets	213,407,453
MiDaS-tf-Swin2-B384-102M [7]‡	supervised	Transformer	-	-	10 datasets	102,378,913
MiDaS-tf-Swin2-L384-213M [7]‡	supervised	Transformer	-	-	10 datasets	213,411,869
MiDaS-tf-Swin2-T256-42M [7]‡	supervised	Transformer	-	-	10 datasets	41,701,331
MiDaS-hy-H384-123M [44]‡	supervised	hybrid	-	-	10 datasets	123,146,985
MiDaS-hy-H384-123M-K [44]†	supervised	hybrid	✓	-	10 datasets	123,146,985
MiDaS-hy-H384-123M-N [44]	supervised	hybrid	-	✓	10 datasets	123,146,985
MiDaS-cn-L384-344M [44]‡	supervised	CNN	-	-	10 datasets	344,055,465
MiDaSv21-cn-L384-105M [43]‡	supervised	CNN	-	-	6 datasets	105,362,945
MiDaSv21-cn-S256-21M [43]‡	supervised	CNN	-	-	6 datasets	21,320,545
MIM-tf-87M-K [58]	supervised	Transformer	✓	-	-	87,219,257
MIM-tf-87M-N [58]	supervised	Transformer	-	✓	-	87,219,257
NeWCRFs-tf-K [67]	supervised	Transformer	✓	-	-	270,444,877
NeWCRFs-tf-N [67]	supervised	Transformer	-	✓	-	270,444,877
Omnidata-tf [10]†	supervised	Transformer	-	-	7 datasets	123,146,985
P2Net-cn-3frames [66]‡	self-supervised	CNN	-	✓	-	14,840,217
P2Net-cn-5frames [66]‡	self-supervised	CNN	-	✓	-	14,840,217
PackNet-cn [16]†	self-supervised	CNN	✓	-	-	128,294,020
SCDepth-v1-cn-D [6]†	self-supervised	CNN	-	-	DDAD	14,842,236
SCDepth-v1-cn-K [6]†	self-supervised	CNN	✓	-	-	14,842,236
SCDepth-v2-cn-N [5]†	self-supervised	CNN	-	✓	-	14,842,236
SCDepth-v3-cn-B [49]†	hybrid (disparity)	CNN	-	-	Bonn	14,842,236
SCDepth-v3-cn-D [49]†	hybrid (disparity)	CNN	-	-	DDAD	14,842,236
SCDepth-v3-cn-K [49]†	hybrid (disparity)	CNN	✓	-	-	14,842,236
SCDepth-v3-cn-N [49]†	hybrid (disparity)	CNN	-	✓	-	14,842,236
SCDepth-v3-cn-T [49]†	hybrid (disparity)	CNN	-	-	TUM	14,842,236
StructDepth-cn [34]‡	self-supervised	CNN	-	✓	-	14,840,217
TrainFlow-cn-K [69]	self-supervised	CNN	✓	-	-	19,974,541
TrainFlow-cn-N [69]	self-supervised	CNN	-	✓	-	19,974,541
TransDepth-hy-K [60]	supervised	hybrid	✓	-	-	247,399,587
TransDepth-hy-N [60]	supervised	hybrid	-	✓	-	247,399,587
ZeroDepth-tf [17]	supervised	Transformer	-	-	5 datasets	232,591,380
ZoeDepth-tf-K [4]	supervised	Transformer	✓	-	10 datasets	344,820,487
ZoeDepth-tf-N [4]	supervised	Transformer	-	✓	10 datasets	334,816,746
ZoeDepth-tf-NK [4]	supervised	Transformer	✓	✓	10 datasets	346,100,355

DDAD [16]. Mixed-domain models such as MiDaS [43, 44] and ZoeDepth [4] were pretrained on large composite datasets (e.g., MIX6, MIX10) combining synthetic and real imagery from diverse sources. Depth-Anything [61] and Metric3D [65] further extend this paradigm by integrating numerous labeled and pseudo-labeled datasets across both indoor and outdoor environments.

All pretrained weights were obtained from publicly available repositories. Minimal code adjustments were made solely to ensure compatibility with our hardware (GALLERIA UL9C-R49-6, RTX 4090 GPU) without altering model architectures or pretrained parameters. Model suffixes indicate dataset and architectural variations: ‘-K’, ‘-N’, ‘-B’, ‘-D’, and ‘-T’ correspond to KITTI, NYU, Bonn, DDAD, and TUM, respectively; ‘-NK’ denotes dual fine-tuning on KITTI and NYU. Backbone abbreviations include ‘cn’ (CNN), ‘tf’ (Transformer), ‘hy’ (hybrid), and ‘df’ (diffusion). Parameter counts are expressed as, for example, ‘-49M’ or ‘-87M’.

For evaluation consistency, DNN outputs were categorized as absolute depth, scale-shift invariant relative depth (\dagger), or disparity (\ddagger), stored in 16-bit (uint16) format. When we calculated scale-recovered data from DNN outputs, we performed per-image linear regression between predictions (z_{out}) and ground truth (z_{GT}) for sixteen evaluation points, fitting $z_{\text{GT}} = s * z_{\text{out}} + t$ to estimate optimal scaling (s^*) and shifting (t^*) factors. Transformed outputs were computed as $z'_{\text{out}} = s^* * z_{\text{out}} + t^*$. For disparity-based models, we first applied the same regression to recover pseudo-absolute disparity and inverted the resulting values to obtain pseudo-absolute depth. Negative disparities (rare outliers) were clipped to zero. We found that this linear regression normalization tend to yield more stable depth alignment than alternative median-based normalization methods [43].

B. Supplemental Results

B.1. Affine coefficients and residual errors

To examine whether DNNs exhibit human-like affine biases at the per-image level, we estimated four affine coefficients—scale (a_z), shift (b), horizontal shear (a_x), and vertical shear (a_y)—using the affine decomposition analysis described in Section 3.4. The decomposition was conducted for both human observers and DNNs on the sixteen evaluation points per image. The results of this analysis are summarized in Figure B1 (absolute data) and Figure B2 (scale-recovered data), which show the mean coefficients for each model, averaged across all evaluation images.

Overall, most DNNs exhibited $a_z < 1.0$ and $b > 0.0$, indicating a depth compression effect at greater distances. As expected, NYU-trained DNNs (red and orange) displayed particularly small a_z values, reflecting their tendency to estimate depth with the fixed scale range inherent to the NYU dataset. In contrast, human data showed markedly large positive b values, suggesting that the perceived viewpoint is effectively shifted backward relative to the physical camera position. This systematic offset likely reflects a perceptual bias associated with viewing wide-angle images, wherein distant regions are perceived as farther away than they physically are [26].

For the horizontal shear coefficient (a_x), most DNNs exhibited only minor or negligible systematic biases. However, both humans and several DNNs showed a negative shift, indicating that the right side of the image tended to appear as closer than its physical depth. The vertical shear coefficient (a_y) revealed a pronounced negative bias in human data, where the lower portion of the image tended to appear closer than it actually was. DNNs displayed a similar but weaker tendency, suggesting that they partially replicate “lower-region bias” of humans [21, 28, 52]. These shearing biases are consistent with the explanation discussed in the main manuscript: Geometric asymmetries derived from the KITTI dataset may systematically influence the spatial bias observed in both human and DNNs.

For residual errors, the NYU-trained models exhibited smaller residuals than both the KITTI-trained models and human data. However, this reduction primarily reflects the mathematical characteristics of our affine fitting procedure—specifically, the residual RMSE was computed within each DNN’s training depth range (e.g., 0-10 m for NYU and 0-80 m for KITTI). Therefore, a smaller residual does not necessarily indicate higher accuracy in representing real-world depth geometry. Focusing on the human data, human observers showed residual errors comparable to those of KITTI-trained models, suggesting that, in terms of residual magnitude alone, humans behave similarly to high-performing DNNs within the affine-invariant representation, despite distinct estimation strategies described in the main manuscript.

B.2. Quantifying trade-off relationships between accuracy and human-likeness

Table B1 provides a quantitative summary of the trade-off between metric accuracy and human similarity for both absolute and scale-recovered data. For each condition, we computed the Pearson correlation between log-RMSE (scale-shift invariant RMSE on a log scale) and human similarity, separately for the raw errors and affine components within the human-superior and human-inferior groups. As described in the main manuscript, nearly all measures exhibit trade-off patterns. Especially,

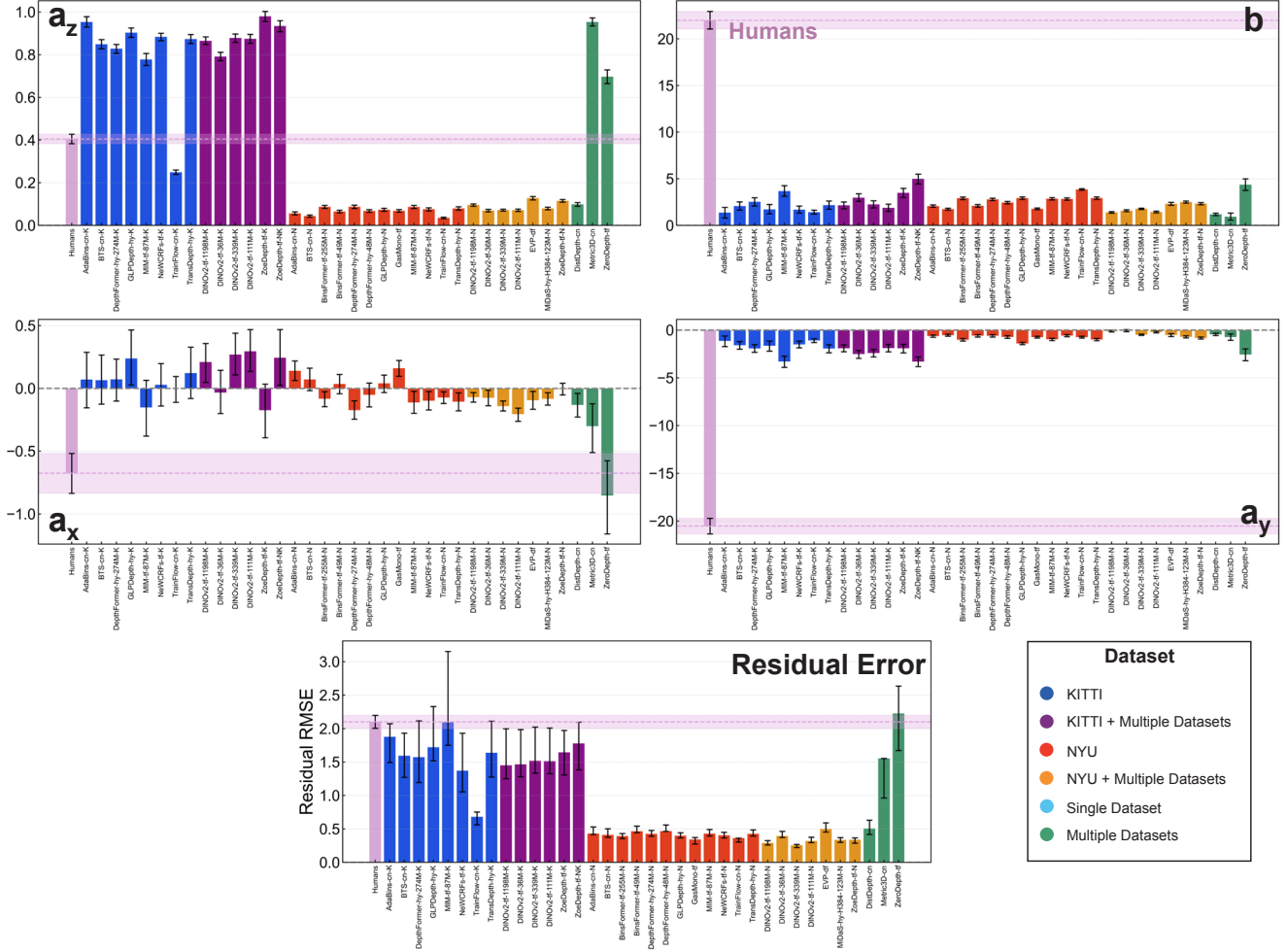


Figure B1. Affine coefficients and residual error for humans and 36 DNNs that output absolute depth. The figure consists of five subplots: scale component (a_z), shift component (b), horizontal shear component (a_x), vertical shear component (a_y), and the residual error component.

Table B1. Quantitative analysis of trade-off relationships. Pearson correlation coefficients were computed between log-RMSE and human-similarity scores to quantify the trade-off between metric accuracy and perceptual alignment. Statistical significance is denoted by asterisks: * : $p < 0.05$ ** : $p < 0.01$, and *** : $p < 0.001$.

Measures	Absolute Data		Scale-Recovered Data	
	Human-Superior Group	Human-Inferior Groups	Human-Superior Group	Human-Inferior Groups
Model Numbers	17	19	22	47
Raw Error	$r = 0.37; p = 0.14$	$r = -0.22; p = 0.38$	$r = 0.69^{***}; p < 0.001$	$r = -0.56^{***}; p < 0.001$
a_z	$r = 0.41; p = 0.10$	$r = -0.69^{***}; p < 0.001$	$r = 0.33; p = 0.14$	$r = -0.56^{***}; p < 0.001$
b	$r = 0.32; p = 0.21$	$r = -0.79^{***}; p < 0.001$	$r = 0.42^*; p = 0.05$	$r = -0.44^{***}; p < 0.001$
a_x	$r = 0.44; p = 0.07$	$r = -0.84^{***}; p < 0.001$	$r = 0.47^*; p = 0.03$	$r = -0.68^{***}; p < 0.001$
a_y	$r = 0.50^*; p = 0.04$	$r = -0.84^{***}; p < 0.001$	$r = 0.48^*; p = 0.03$	$r = -0.50^{***}; p < 0.001$
Residual Error	$r = 0.63^{**}; p = 0.007$	$r = -0.88^{***}; p < 0.001$	$r = 0.64^{**}; p = 0.001$	$r = -0.66^{***}; p < 0.001$

the scale-recovered data and affine components exhibit a clear inverse-U relationship. Most interestingly, models with accuracy close to the human level accuracy display the highest alignment with human depth estimates, whereas models surpassing

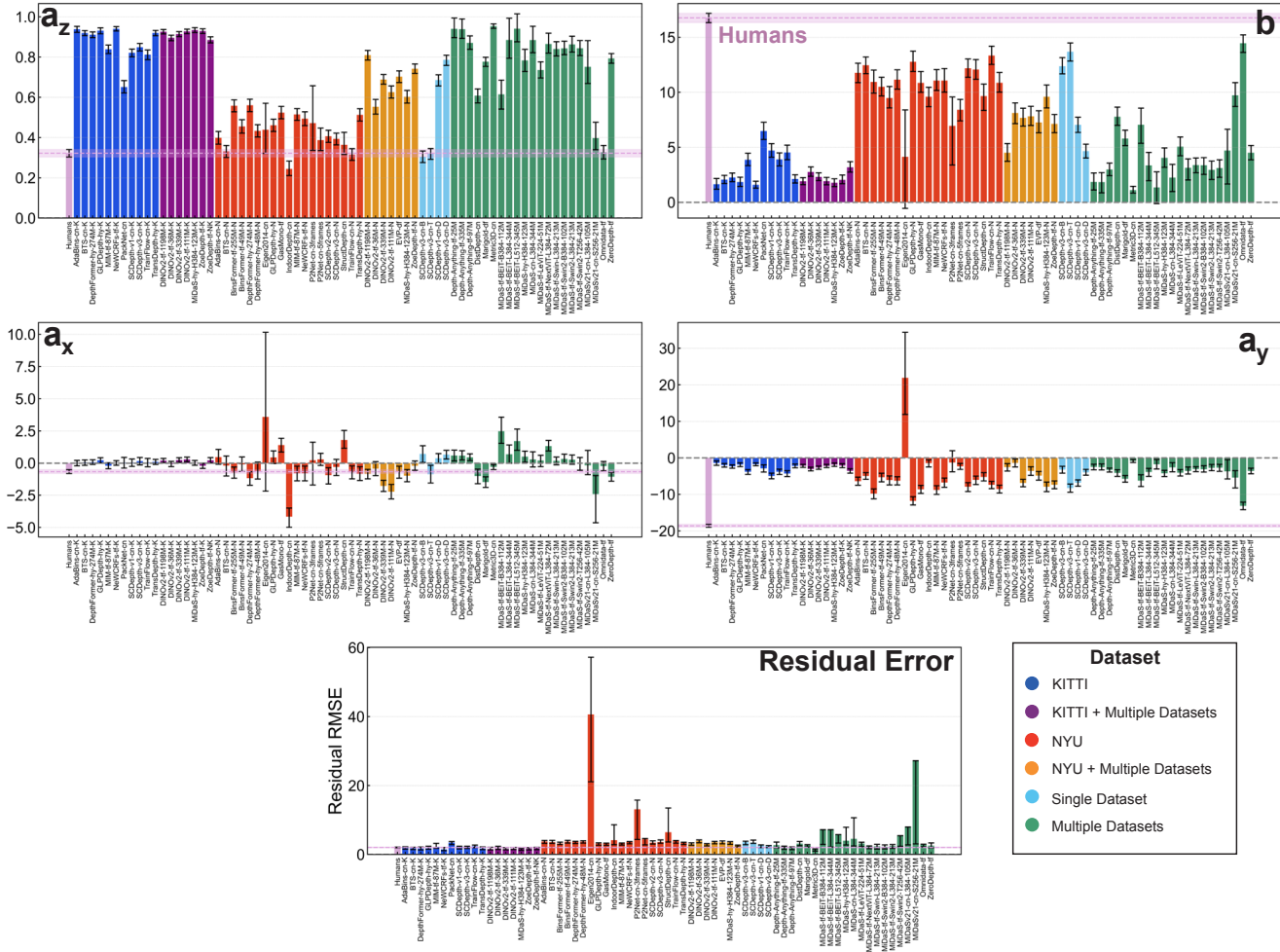


Figure B2. Affine coefficients and residual error for humans and 69 DNNs for scale-recovered data. The figure consists of five subplots: scale component (a_z), shift component (b), horizontal shear component (a_x), vertical shear component (a_y), and the residual error component.

human accuracy tended to diverge from human-like error structures.

B.3. Consistency of human-likeness ranking among raw error and affine components

To determine whether the inverse-U relationships observed in Figures 2C and 3 were driven by similar human-similarity model rankings, we compared them across the raw error and affine components using Spearman rank correlations. Specifically, we first computed the human-similarity ranking for each component—across 36 DNNs for the absolute data and 69 DNNs for the scale-recovered data—and then examined how consistently these rankings were preserved across components by computing pairwise Spearman rank correlations among them. As summarized in Figure B3, similarity rankings were strongly correlated across the affine coefficients and the residual error for both the absolute and the scale-recovered analyses, whereas the raw-error rankings showed relatively weak correlation with these components. These findings indicate that the clear inverse-U patterns for the affine coefficients and the residual error are organized by a largely shared ordering of DNNs, while the raw-error patterns reflects a distinctive structure.

B.4. Comparing individual datasets and backbone variations

To better understand the variability in human-DNN similarity, we investigated factors beyond overall accuracy that may influence the alignment of their error patterns. We first examined the role of training data by comparing DNNs with iden-

Model Ranking Correlation

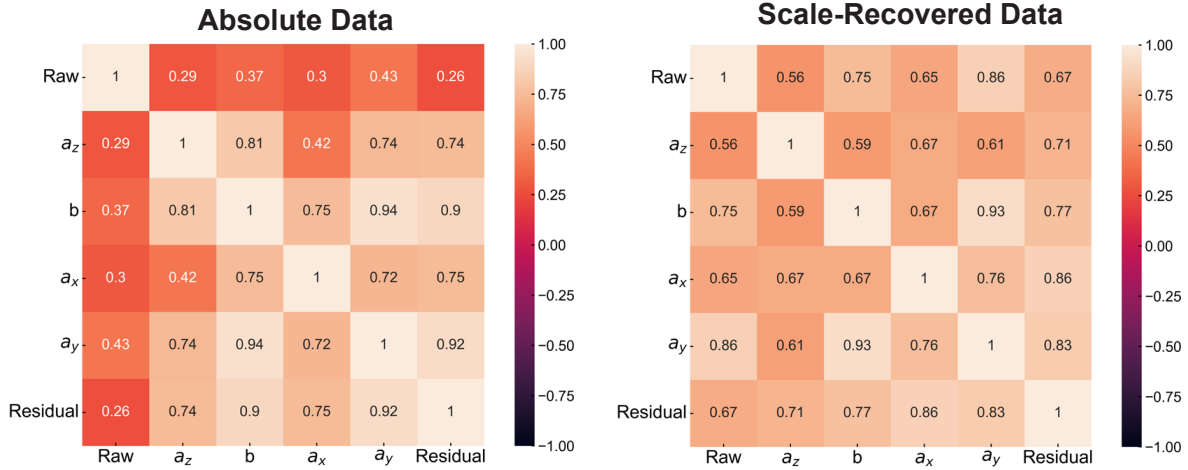


Figure B3. Spearman rank correlations showing the consistency of human-similarity rankings across the raw error and affine components for (A) absolute data and (B) scale-recovered data.

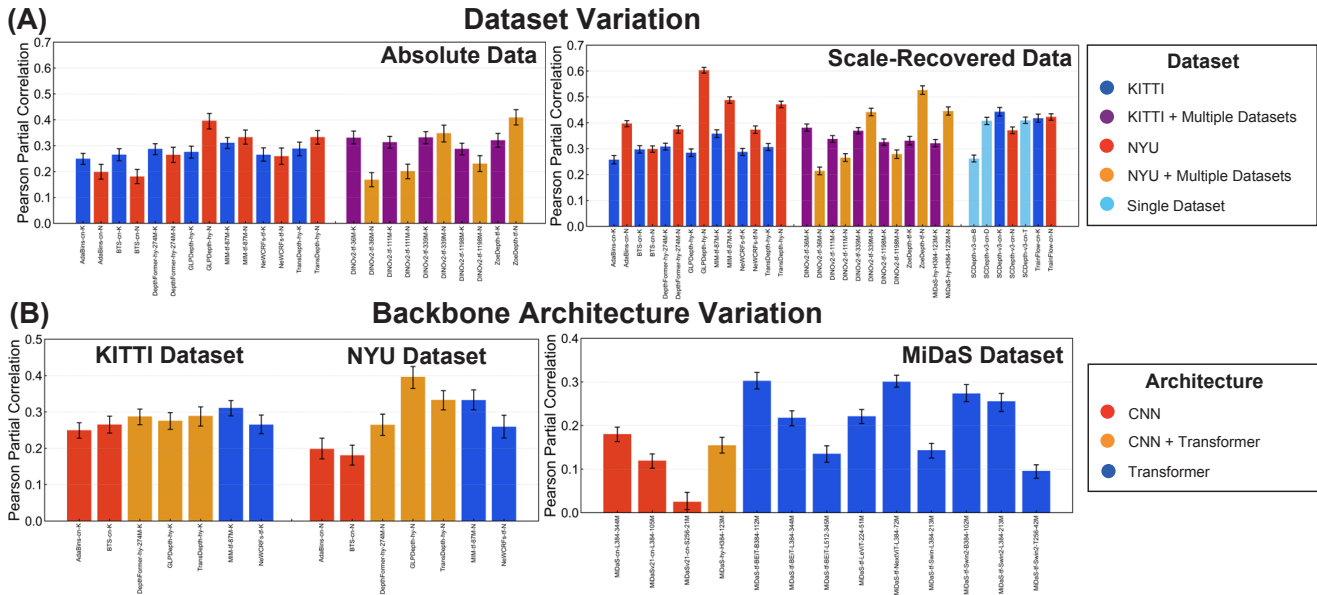


Figure B4. Human-DNN similarity across selected models. (A) Variation across different training datasets, with colors indicating the dataset type. (B) Variation across different backbone architectures, with colors indicating the architecture type.

tical architectures but trained on different datasets. Among supervised models (AdaBins [3], BTS [33], DepthFormer [35], GLPDepth [23], NeWCRFs [67], TransDepth [60]), no consistent trend was observed (Figure B4A). In some cases (e.g., AdaBins and BTS), training on KITTI (in-distribution outdoor data; blue) increased human similarity, whereas in others (e.g., GLPDepth and TransDepth), training on NYU (out-of-distribution indoor data; red) yielded stronger correspondence with human estimates. A similarly mixed pattern was found among DNNs pretrained on multiple datasets and fine-tuned on either KITTI or NYU (purple and orange; DINOv2 [40], ZoeDepth [4], MiDaS [44]). These nuanced results indicated that the choice of training dataset alone cannot explain differences in human similarity.

Next, we assessed the influence of learning strategies by analyzing the SCDepth-v3 family [49], which employs disparity-

based self-supervision—a biologically plausible alternative to depth-label supervision (right column, Figure B4A). While such training might be expected to enhance human-likeness, the results were again complicated. SCDepth-v3 models fine-tuned on KITTI, as well as several others trained on different datasets, achieved similarly high human similarity, suggesting that certain self-supervised mechanisms can capture human-like error tendencies even under out-of-domain training. However, when considering the broader set of self-supervised DNNs, no consistent advantage in human similarity emerged—some models performed remarkably well, whereas others fell below supervised baselines. This variability underscores that self-supervision alone does not guarantee human-like depth estimation behavior.

Finally, we evaluated the effect of backbone architecture by comparing (1) DNNs fine-tuned on the same KITTI or NYU dataset but differing in backbone design, and (2) MiDaS-family models trained on identical mixed datasets yet implemented with distinct architectures. As shown in Figure B4B, differences in architecture produced only moderate variation in human similarity. Nonetheless, a subtle trend was apparent: Transformer-based models exhibited a slight advantage over CNNs, with mid-sized architectures often achieving the highest similarity. Overall, these results suggest that while architectural choices can produce subtle differences, they are not the primary factor determining the alignment between DNN and human depth-estimation patterns.

B.5. Examples of human estimation biases

We provide additional qualitative examples illustrating how human and DNN per-image depth biases distribute (Figures B5–B8). These figures extend the analyses presented in the main manuscript by highlighting cases that evoke characteristic horizontal (a_x) and vertical (a_y) shear coefficients observed in human data. In each figure, the upper three rows depict scenes eliciting positive or minimal shear, whereas the lower three rows show cases with negative or maximum shear. Together, these examples reveal how both humans and DNNs systematically distort depth in response to specific spatial layouts and object configurations.

For the scale-recovered data, we compared GLPDepth-N—the most human-like among the 69 scale-recovered models—with the state-of-the-art NeWCRFs-K model. Surprisingly, as shown in Figures B7–B8, human-like model (GLPDepth-N)—despite never being exposed to any human data—closely approximates the image-wise distribution of depth biases observed in human perception, capturing scene-dependent patterns of over- and underestimation with somewhat fidelity. In contrast, SOTA model (NeWCRFs-K) shows limited correspondence with these perceptual bias patterns, exhibiting flatter and less human-like error characteristics. This finding highlights that accuracy does not guarantee human-likeness of monocular depth estimators, suggesting the need for human-centric evaluation.

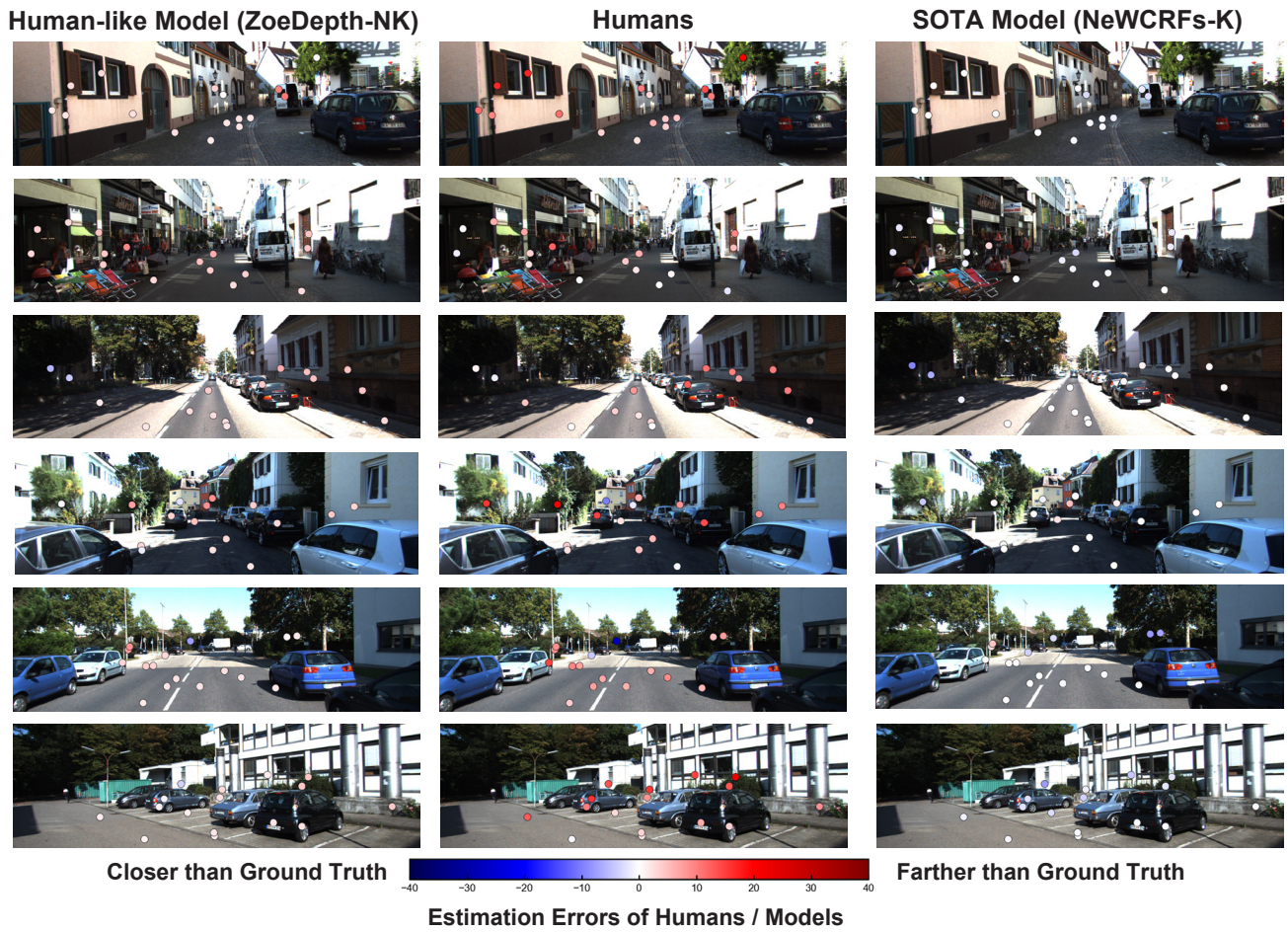


Figure B5. Additional comparison of human and DNN depth estimation biases for the absolute data, illustrated with examples of strong horizontal shear (a_x). Top-three rows show example scenes inducing positive horizontal shear ($a_x > 0$). Bottom-three rows show example scenes inducing negative horizontal shear ($a_x < 0$).

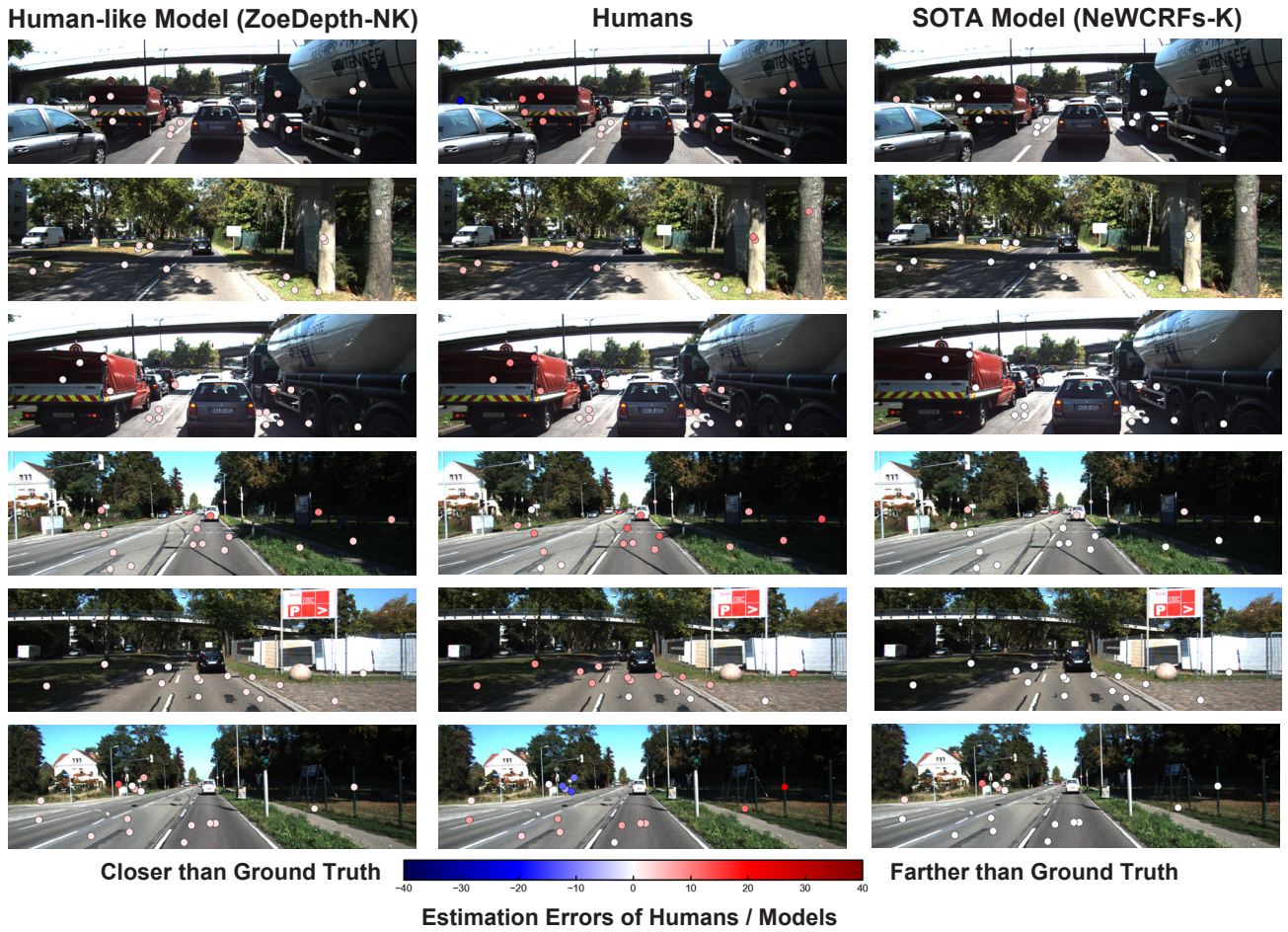


Figure B6. Additional comparison of human and DNN depth estimation biases for the absolute data, illustrated with examples of strong horizontal shear (a_y). Top-three rows show example scenes inducing minimum horizontal shear ($a_y \simeq 0$). Bottom-three rows show example scenes inducing maximum horizontal shear ($a_y < 0$).

Human-like Model (GLPDepth-N)

Humans

SOTA Model (NeWCRFs-K)



Closer than Ground Truth

-40 -30 -20 -10 0 10 20 30 40

Farther than Ground Truth

Estimation Errors of Humans / Models (scale-recovered)

Figure B7. Additional comparison of human and DNN depth estimation biases for the scale-recovered data, illustrated with examples of strong horizontal shear (a_x). Top-three rows show example scenes inducing positive horizontal shear ($a_x > 0$). Bottom-three rows show example scenes inducing negative horizontal shear ($a_x < 0$).

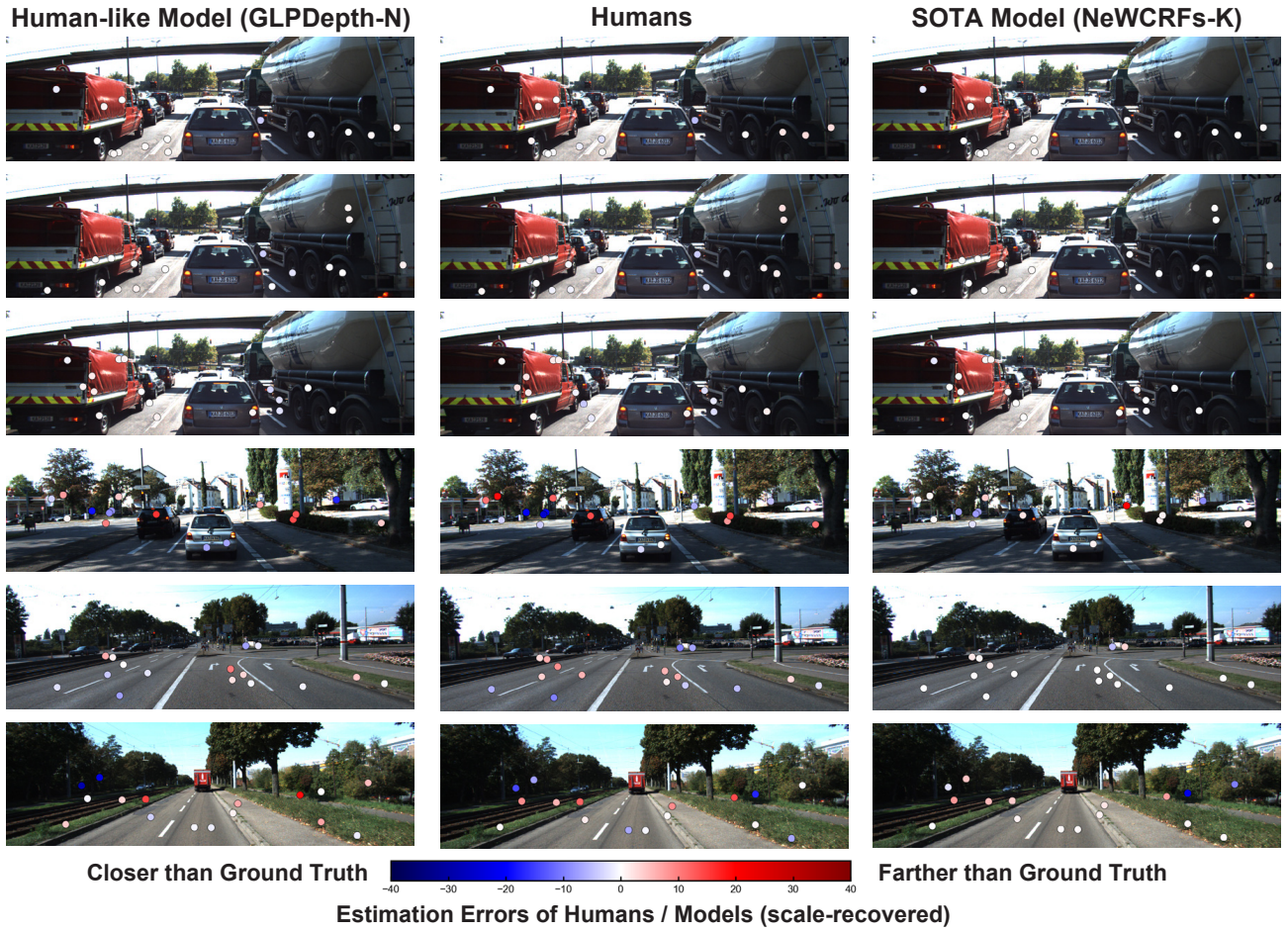


Figure B8. Additional comparison of human and DNN depth estimation biases for the scale-recovered data, illustrated with examples of maximum and minimum horizontal shear (a_y). Top-three rows show example scenes inducing minimum horizontal shear ($a_y \simeq 0$). Bottom-three rows show example scenes inducing maximum horizontal shear ($a_y < 0$).